JAASCI
http://jaasci.com
JOURNAL OF ADVANCED APPLIED SCIENCES
e-ISSN: 2979-9759
PRENSIP
https://prensip.gen.tr

RESEARCH ARTICLE

Characterization of Positive and Negative Ionospheric Storm Phases Using TNPGN-Active TEC Estimates Spanning Solar Cycles 24 and 25 (2019-2023)[*]

Secil Karatay[1]✉ • Feza Arikan[2] • Orhan Arikan[3]

[1]Kastamonu University, Faculty of Engineering and Architecture, Department of Electrical Electronics Engineering, Kastamonu/Türkiye
[2]Hacettepe University, Faculty of Engineering, Department of Electrical Electronics Engineering, Ankara/Türkiye
[3]İhsan Doğramacı Bilkent University, Faculty of Engineering, Department of Electrical Electronics Engineering, Ankara/Türkiye

ARTICLE INFO

Article History
Received: 13.04.2026
Accepted: 15.06.2026
First Published: 28.06.2026

Keywords
Geomagnetic storm
GNSS-TEC
Ionospheric storm
Mid-latitude ionosphere
Solar Cycle 24-25
TNPGN-Active

ABSTRACT

Geomagnetic storms induce significant perturbations in the ionosphere, profoundly affecting Total Electron Content (TEC) and consequently the performance of Global Navigation Satellite Systems (GNSS). This study characterizes the positive and negative phases of ionospheric storms over Türkiye during 14 geomagnetically disturbed days (maximum 3-hourly Kp > 6, corresponding to G2–G4 storms on the NOAA scale) spanning January 2019 to June 2023. The period covers the deep minimum of Solar Cycle 24 (SC24) and the ascending phase of Solar Cycle 25 (SC25). High-resolution IONOLAB-TEC estimates at 2.5-minute intervals are derived from nine continuously operating stations of the Turkish National Permanent GNSS Network-Active (TNPGN-Active). These stations, distributed across geodetic latitudes 36.59°N-42.01°N and longitudes 26.33°E-44.34°E, provide comprehensive spatial coverage of the mid-latitude ionosphere over the Eastern Mediterranean and Anatolian region. A single geomagnetically quiet reference day (07 May 2022) is selected and an observation-driven pre-storm scaling procedure is applied to normalize the TEC time series. This approach effectively accounts for seasonal and solar-cycle differences in background ionization levels without dependence on empirical models. Analysis of network-averaged normalized TEC deviations ($r\Delta TEC$) reveals that storm responses are governed by a complex interplay of factors. Storm intensity provides a first-order control on perturbation magnitude, with G4 events generally producing larger peak positive deviations. However, the local time of storm onset strongly modulates phase dominance: near-noon onsets favor prolonged negative phases associated with thermospheric composition changes, while midnight-to-morning onsets promote extended positive phases driven by prompt penetration and disturbance dynamo electric fields. Seasonal dependence is pronounced, with spring events displaying the most consistent positive responses, winter conditions amplifying relative enhancements due to lower baseline TEC and summer suppressing both phases. Pre-storm scaling factors clearly reflect the solar-cycle transition, showing a roughly twofold increase in background TEC from the SC24 minimum to early SC25. These results establish a regional observational baseline for mid-latitude ionospheric storm morphology in an underrepresented longitude sector. They highlight the value of dense GNSS networks and observation-based normalization techniques for advancing space weather understanding and improving GNSS reliability as Solar Cycle 25 approaches its maximum.

Please cite this paper as follows:

Karatay, S., Arikan, F., & Arikan, O. (2026). Characterization of positive and negative ionospheric storm phases using TNPGN-Active TEC estimates spanning Solar Cycles 24 and 25 (2019-2023). *Journal of Advanced Applied Sciences*, *5*(1), 8-23. https://doi.org/10.61326/jaasci.v5i1.481

1. Introduction

The ionosphere, a dynamic layer of Earth's upper atmosphere extending roughly from 60 to 1000 km altitude, plays a critical role in modulating the propagation of radio waves, particularly those used by Global Navigation Satellite Systems (GNSS) (Hernández-Pajares, et al., 2011; Jakowski, et al., 2012; Ren, et al., 2016). Total Electron Content (TEC), defined as the integrated number of free electrons along a signal path through the ionosphere (typically expressed in TEC units, where 1 TECU = 10^{16} electrons/m^2), directly influences the refractive index experienced by L-band GNSS signals (Arikan,

---

[*] A supplementary file for this article is available at https://doi.org/10.61326/jaasci.v5i1.481

✉ Correspondence
E-mail address: skaratay@kastamonu.edu.tr

et al., 2003; Nayir, et al., 2007). This leads to group delay and phase advance effects that can introduce positioning errors ranging from meters to tens of meters if not properly modeled or corrected (Arikan, et al., 2008). Under geomagnetically quiet conditions, the ionosphere exhibits predictable diurnal, seasonal, and solar-cycle variations driven primarily by solar Extreme Ultra Violet (EUV) radiation (Vaishnav, et al., 2019), neutral winds (Lu, et al., 1995) and background electric fields (Pudovkin, 1974). However, during periods of heightened geomagnetic activity, triggered by Coronal Mass Ejections (CMEs), high-speed solar wind streams, or other solar wind structures interacting with Earth's magnetosphere, the ionosphere undergoes rapid and often dramatic perturbations known as ionospheric storms (Fuller-Rowell, et al., 1994; Lei, et al., 2008; Lyon, 2000; Ridley, et al., 2006a).

Geomagnetic storms are quantified through indices such as the planetary Kp (measuring global geomagnetic disturbance on a 0–9 scale) (GFZ, 1956), the Disturbance storm time (Dst) index (reflecting the intensity of the equatorial ring current) and the high-resolution SYM-H index (a one-minute analogue of Dst (WDC, 1957) When the Interplanetary Magnetic Field (IMF) turns southward, efficient magnetic reconnection at the dayside magnetopause allows solar wind energy to penetrate the magnetosphere, leading to enhanced convection electric fields, Joule heating in the high-latitude thermosphere and the generation of disturbance dynamo electric fields (Maruyama, et al., 2005; Sojka, et al., 1986; Vasyliūnas & Song, 2005; Yu & Ridley, 2009). These processes cascade downward, altering thermospheric composition (notably the O/N_2 ratio), neutral winds and plasma transport at mid-latitudes (Rishbeth & Garriott, 1969). The resulting ionospheric responses manifest as either positive phases (enhancements in electron density and TEC, often driven by prompt penetration electric fields or equatorward neutral winds that uplift plasma to altitudes of reduced recombination) or negative phases (depletions in TEC, typically linked to changes in thermospheric composition where molecular-rich air is transported equatorward, increasing recombination rates) (Fagundes, et al., 2016; Jin, et al., 2017; Mishin, et al., 2019; Ridley, et al., 2006b). These phases do not occur uniformly; their dominance, timing, duration and spatial extent depend on a complex interplay of factors including the storm's intensity and duration, the local time of onset, season, longitude and the prevailing level of solar activity. Storms commencing near local midnight or in the morning sector at mid-latitudes frequently favor prolonged positive responses due to favorable electric field configurations (Huang, et al., 2005; Wang, et al., 2010), whereas daytime-onset events (especially near local noon) tend to promote composition-driven negative phases (Akala, et al., 2023; Gulyaeva & Stanislawska, 2005). Seasonal asymmetries arise from differences in background thermospheric circulation and background plasma density: winter conditions often amplify relative TEC enhancements because of lower baseline densities (Yasyukevich, et al., 2020), while summer solstice periods can suppress both positive and negative responses due to less favorable neutral composition (Gulyaeva, et al., 2014; Karatay, et al., 2017; Karatay, 2020c). Longitudinal variations further complicate the picture, as the offset between geographic and geomagnetic coordinates influences the efficiency of energy deposition and plasma redistribution (Karatay, 2020a; Karatay, 2020b).

The transition from Solar Cycle 24 (SC24) to Solar Cycle 25 (SC25) offers a particularly valuable observational window for such studies. SC24 was notably weak, with a prolonged and deep minimum characterized by unusually low sunspot numbers, reduced EUV flux and subdued geomagnetic activity (Richardson, 2013; Watari, 2017). In contrast, the ascending phase of SC25 has shown a more robust increase in solar activity, with a higher frequency of intense geomagnetic events in 2021–2023 compared to the preceding minimum years (Hajra, et al., 2021; Javaraiah, 2022; Upton & Hathaway, 2023). This progression allows examination of how ionospheric storm morphology evolves with changing background solar flux levels, as higher EUV illumination elevates the ambient F-region plasma density and alters the ionosphere's susceptibility to external forcing (Yeeram, 2024). Multi-year analyses spanning this transition thus help disentangle solar-cycle modulation from pure geomagnetic drivers.

Mid-latitude regions, situated between the Equatorial Ionization Anomaly (EIA) and auroral zones, serve as sensitive indicators of these coupled magnetosphere–ionosphere–thermosphere processes. Unlike equatorial latitudes, where fountain-effect amplification and plasma bubbles dominate, or high latitudes dominated by particle precipitation and convection, mid-latitudes experience a balanced influence from both prompt penetration fields and longer-lived disturbance dynamo effects, as well as equatorward-propagating thermospheric disturbances (Wehmeyer, et al., 2026; Yi Liu, et al., 2021). Over the Eastern Mediterranean and Anatolian plateau, the ionosphere lies in a transitional zone influenced by European, African and Asian longitudinal sectors, making it responsive to both hemispheric asymmetries and regional geomagnetic field geometry (Doğanalp & Köz, 2024; Ghafar, et al., 2024). Türkiye, spanning geodetic latitudes approximately 36°N to 42°N and longitudes 26°E to 44°E, provides excellent geographic coverage of this mid-latitude domain. Its position allows investigation of spatial gradients across nearly 18° of longitude, capturing variations that may arise from differences in magnetic declination, local time sectors and proximity to the mid-latitude trough during disturbed conditions (Erken, et al., 2019; Karatay, et al., 2017; Karatay, 2020a; Karatay, 2020b; Karatay, 2020c).

Previous regional studies in the Eastern Mediterranean and surrounding areas have documented ionospheric storm effects using various techniques, including ionosondes (Haralambous

& Makrominas, 2024; Paul, et al., 2025; Pietrella, et al., 2018), GNSS networks and satellite observations (Campuzano, et al., 2023; Pica, et al., 2025; Şentürk, 2020). These works have highlighted the occurrence of both positive and negative phases, their dependence on storm onset local time and occasional preconditioning effects during consecutive storm sequences. However, comprehensive analyses employing dense, continuously operating GNSS reference networks, such as the Turkish National Permanent GNSS Network-Active (TNPGN-Active), remain relatively limited for the SC24/SC25 transition period, particularly when focusing on events selected by consistent intensity thresholds (e.g., Kp ≥ 6, corresponding to G2 or stronger on the National Oceanic and Atmospheric Administration (NOAA) scale). Such networks enable high-temporal-resolution (e.g., 2.5-minute) TEC estimation across multiple stations, facilitating network-averaged characterizations that reduce local noise and reveal regional coherence or variability (Arikan, et al., 2016; Koroglu & Arikan, 2025).

Understanding ionospheric responses over Türkiye carries both scientific and practical significance (Karatay, et al., 2017; Karatay, 2020a; Karatay, 2020b; Karatay, 2020c). Scientifically, it contributes to global models of storm-time ionospheric dynamics by filling a data gap in a longitude sector underrepresented in many statistical studies. Practically, reliable TEC characterization is essential for mitigating GNSS errors in applications ranging from precise point positioning and real-time kinematic surveying to aviation, maritime navigation and satellite-based augmentation systems. During geomagnetic storms, unmodeled TEC gradients and scintillations can degrade positioning accuracy, increase cycle slips and even cause signal loss-of-lock, with economic and safety implications (Koroglu & Arikan, 2025). Moreover, as solar activity rises toward the SC25 maximum, the frequency and intensity of such disturbances are expected to increase, underscoring the need for observation-based benchmarks derived from regional GNSS infrastructure.

This study leverages IONOLAB-TEC estimates from nine TNPGN-Active stations distributed across distinct geographic zones of Türkiye to analyze the ionospheric response during 14 geomagnetically disturbed days (selected on the basis of maximum 3-hourly Kp > 6) between January 2019 and June 2023. These events encompass a range of intensities (G2 to G4), seasonal contexts and solar activity backgrounds, spanning the late minimum of SC24 and the ascending phase of SC25. A single geomagnetically quiet reference day is employed in conjunction with an observation-driven pre-storm scaling procedure to normalize IONOLAB-TEC time series, thereby isolating storm-induced deviations while accounting for seasonal and solar-cycle differences in background levels. The analysis examines absolute and relative TEC deviations, network-mean responses, peak positive/negative excursions, phase durations and statistical distributions stratified by storm class and season. By integrating supporting geomagnetic indices (Kp, Dst, SYM-H) (GFZ, 1956; WDC, 1957) and focusing on spatial averaging across the Anatolian network, the work aims to elucidate the dominant controlling factors, storm intensity, onset timing, season and solar background, on mid-latitude ionospheric storm morphology in this region.

2. Materials and Methods

This study analyzes the ionospheric response over Türkiye during geomagnetically disturbed periods using TEC estimates derived from nine continuously operating GNSS reference stations of the TNPGN-Active. The stations are distributed across nine distinct geographic zones of Türkiye, spanning geodetic latitudes from 36.59°N to 42.01°N and longitudes from 26.33°E to 44.34°E (Table 1), thereby providing spatial coverage of the mid-latitude ionosphere over the Eastern Mediterranean and Anatolian region. The geographic locations of the selected stations are shown in Figure 1.

The study period covers January 2019 to June 2023, encompassing the deep minimum of Solar Cycle 24 (SC24) and the ascending phase of Solar Cycle 25 (SC25). Geomagnetically disturbed days are selected based on the planetary Kp index, provided by the German Research Centre for Geosciences (GFZ Potsdam) (GFZ, 1956). Days on which the maximum 3-hourly Kp value exceeded 6, corresponding to at least a G2-class geomagnetic storm on the NOAA scale, are included in the analysis. This criterion yielded 14 disturbed days ranging from G2 to G4 in storm intensity, as listed in Table 2. The selected events include storms occurring across all four seasons and under varying solar activity levels, enabling an assessment of seasonal and solar-cycle effects on the ionospheric storm response (Matzka, et al., 2021). The disturbance storm time (Dst) index and the SYM-H index were obtained from the World Data Center for Geomagnetism, Kyoto (WDC Kyoto) (WDC, 1957).

Table 1. Chosen TNPGN-Active stations located in nine different zones across Türkiye.

Station Name/ID	Latitude (°N)	Longitude (°E)
Adana/ADN2	36.59	35.19
Ardahan/ARDH	41.06	42.41
Boğazlıyan/BOG1	39.11	35.15
Edirne/EDIR	41.40	26.33
Kırkağaç/KIKA	39.06	27.40
Muğla/MUG1	37.12	28.21
Muradiye/MUR1	38.59	43.45
Şemdinli/SEM1	37.18	44.34
Sinop/SINP	42.01	35.09

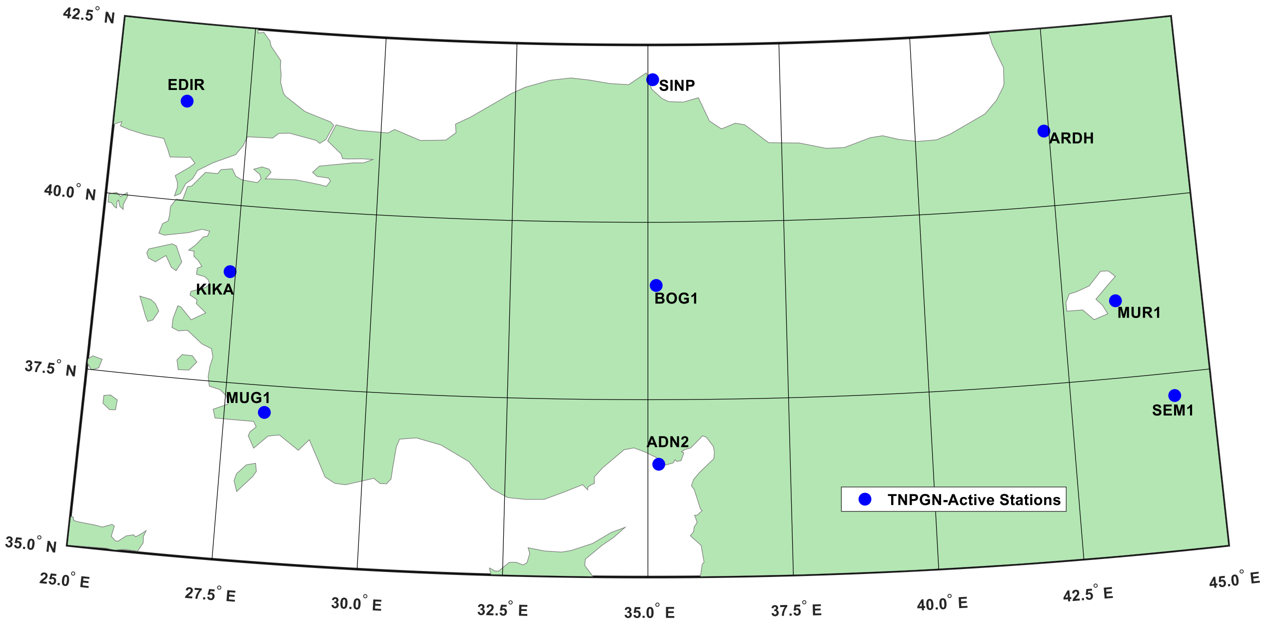

Figure 1. Geographic locations of the TNPGN-Active stations used in the study.

Table 2. Chosen geomagnetically disturbed days and quiet day between 2019-2023.

Geomagnetic Condition	Day	Kp maks.	Class	Season	Onset (UT)
Disturbed days	14 May 2019	6.3	G2	Spring	05:00
	12 May 2021	7.0	G3	Spring	13:00
	12 October 2021	6.3	G2	Autumn	00:00*
	03 November 2021	6.3	G2	Autumn	22:00
	04 November 2021	7.7	G3	Autumn	05:00
	13 March 2022	6.3	G2	Spring	15:00
	10 April 2022	6.6	G2	Spring	06:00
	17 August 2022	6.6	G2	Summer	20:00
	04 September 2022	6.3	G2	Autumn	05:00
	27 February 2023	6.6	G2	Winter	00:00*
	23 March 2023	7.0	G3	Spring	12:00
	24 March 2023	8.0	G4	Spring	00:00
	23 April 2023	8.3	G4	Spring	12:00
	24 April 2023	8.0	G4	Spring	00:00*
Quiet Day	07 May 2022	1.6	—	Spring	05:00

The Class column refers to the NOAA geomagnetic storm scale (G1–G5, Kp ≥ 5); dash indicates no storm condition. Asterisk (*) denotes events for which the storm onset preceded the start of the observational window; a one-hour fallback scaling window was applied as described in Section 2.1.

Dst is a hourly index that quantifies the globally symmetric disturbance of the horizontal geomagnetic field component at equatorial latitudes and is widely used to characterize the intensity and phase of geomagnetic storms (Sugiura, 1964). SYM-H is the one-minute equivalent of Dst, providing higher temporal resolution suitable for identifying the precise onset timing of each storm event (Nakano & Iyemori, 2005). The Kp and Dst time series for all 14 disturbed days, together with the quiet reference day, are presented in Figure 2. The corresponding SYM-H time series are shown in Figure 3. A single geomagnetically quiet day (07 May 2022, $Kp_{max} = 1.33$, $Dst_{min} = -10\ nT$) is selected as the reference baseline for the normalization procedure described in Section 2.1.

2.1. Normalization of IONOLAB-TEC Time Series and Derivation of Ionospheric Storm Response

The IONOLAB-TEC algorithm computes VTEC from dual-frequency GPS observations by forming the geometry-free linear combination of the L1 (1575.42 MHz) and L2 (1227.60 MHz) carrier phase and pseudorange measurements, which eliminates the first-order ionospheric delay while retaining the TEC signal. Differential Code Biases (DCBs) for both satellites and receivers are estimated simultaneously within the regularization framework of the algorithm, following the approach described in Arikan et al. (2003, 2008), thereby avoiding reliance on externally provided DCB products. The 2.5-minute output cadence corresponds to the highest temporal resolution achievable from standard 30-second RINEX observation files through the smoothed carrier-phase leveling procedure implemented in the algorithm and is particularly advantageous for resolving the rapid onset and recovery dynamics of ionospheric storm phases, which can evolve on timescales of tens of minutes.

IONOLAB-TEC provides TEC estimates at 2.5-minute intervals for each station and day. For station u, storm d_s and quiet reference day d_q, the IONOLAB-TEC time series is represented as the column vector:

$$\boldsymbol{x}_{u;d_s,d_q} = \left[x_{u;d_s,d_q}(1) \dots x_{u;d_s,d_q}(n) \dots x_{u;d_s,d_q}(N)\right]^T \qquad (1)$$

where $N = 576$ is the total number of samples per day (24 h × 60 min / 2.5 min) and $n = 1,2,\dots,N$ denotes the sample index.

Since the 14 storm events span multiple years and seasons, the absolute IONOLAB-TEC level of the single quiet reference day (07 May 2022) differs from the pre-storm background of each event due to seasonal variation and solar activity changes across Solar Cycle 25. To account for these differences without relying on empirical models, a pre-storm window scaling factor is computed from observations alone.

For each storm event d_s and station u, the storm onset sample index n_{onset} is determined as the first hourly interval at which the Dst index falls below -30 nT. For events where Dst already satisfies this criterion at $n = 1$ (i.e., the storm commenced on the preceding day), a one-hour window ($n_{onset} = 24$ samples) s used instead. The scaling factor is then defined as:

$$k_{u;d_s} = \frac{\frac{1}{n_{onset}}\sum_{n=1}^{n_{onset}} x_{u;d_s}(n)}{\frac{1}{n_{onset}}\sum_{n=1}^{n_{onset}} x_{u;d_q}(n)} \qquad (2)$$

where the numerator and denominator are the pre-storm means of the storm day and quiet reference day, respectively, computed over the same time window. The one-hour fallback window is a deliberate conservative choice: it retains the largest possible pre-storm sample while remaining strictly prior to any storm-driven TEC perturbation. However, its application to four events (12 October 2021, 27 February 2023, 24 March 2023, 24 April 2023), in which geomagnetic activity had already commenced before the start of the observational window, introduces a potential source of scaling uncertainty. If storm-driven TEC enhancements are already present within this one-hour window, the computed k will be slightly overestimated relative to the true quiet background, leading to a marginally higher TEC_{ref} and consequently a modest underestimation of the positive $r\Delta TEC$ for those events. Conversely, if a negative phase is already underway, k will be slightly underestimated, amplifying the apparent positive deviation. The direction and magnitude of this effect are event-dependent and cannot be fully quantified without multi-day pre-storm TEC data. Nevertheless, the impact on the primary conclusions of this study, storm phase polarity, duration and the relative ordering of events by intensity class and season, is expected to be minor, as the one-hour window captures the diurnal TEC shape sufficiently to constrain the scaling ratio.

The scaled quiet-day reference vector for station u and storm event d_s is then:

$$\boldsymbol{x}^{ref}_{u;d_s} = k_{u;d_s} \cdot \boldsymbol{x}_{u;d_q} \qquad (3)$$

The absolute IONOLAB-TEC deviation is computed as:

$$\Delta\boldsymbol{x}_{u;d_s} = \boldsymbol{x}_{u;d_s} - \boldsymbol{x}^{ref}_{u;d_s} \qquad (4)$$

and the normalized relative deviation, expressed as a percentage, is:

$$r\Delta x_{u;d_s}(n) = \frac{x_{u;d_s}(n) - x^{ref}_{u;d_s}(n)}{x^{ref}_{u;d_s}(n)} \times 100 \qquad (5)$$

Values of $r\Delta x_{u;d_s}(n) > 0$ indicate a positive ionospheric storm phase (IONOLAB-TEC enhancement), while $r\Delta x_{u;d_s}(n) < 0$ indicate a negative phase (IONOLAB-TEC depletion).

To characterize the spatially averaged ionospheric response over Türkiye, the network mean and standard deviation of the relative deviation are computed across all $U = 9$ stations at each time sample:

$$\overline{r\Delta x_{d_s}}(n) = \frac{1}{U}\sum_{u=1}^{U} r\Delta x_{u;d_s}(n) \qquad (6)$$

$$\sigma_{r\Delta x_{d_s}}(n) = \sqrt{\frac{1}{U}\sum_{u=1}^{U}\left[r\Delta x_{u;d_s}(n) - \overline{r\Delta x_{d_s}}(n)\right]^2} \qquad (7)$$

For each storm event and station, the peak positive and peak negative deviations are defined as:

$$r\Delta x^{+}_{u;d_s} = \max_n\left[r\Delta x_{u;d_s}(n)\right], \quad r\Delta x^{-}_{u;d_s} = \min_n\left[r\Delta x_{u;d_s}(n)\right] \qquad (8)$$

These peak values are subsequently used to compare storm responses across geomagnetic storm intensity classes (G2, G3, G4) and seasons.

3. Results and Discussion

This section presents the analysis of ionospheric TEC response over Türkiye during the 14 geomagnetically disturbed days identified in Table 2. The geomagnetic conditions characterizing each event are first examined through the Kp, Dst and SYM-H indices (Figures 2 and 3). The storm-time IONOLAB-TEC estimates and the scaled quiet-day reference are then compared for the most intense event of the study period (Figure 4), followed by a network-wide characterization of the normalized TEC deviation $r\Delta TEC$ (%) across all 14 events (Figure 5). The pre-storm scaling factors, which quantify the seasonal and solar activity differences between each storm day and the quiet reference day, are presented in Figure 6. Finally, the statistical distribution of peak positive and negative ionospheric responses is assessed as a function of storm intensity class and season (Figure 7).

Figure 2 presents the Kp and Dst indices for the 14 selected geomagnetically disturbed days alongside the quiet reference day (07 May 2022) over the period 2019–2023. The selected events span the deep minimum of Solar Cycle 24 and the ascending phase of Solar Cycle 25, with only one event recorded in 2019 (14 May 2019, G2) and no events meeting the Kp > 6 criterion in 2020, reflecting the historically low geomagnetic activity level during the SC24/SC25 transition minimum. Activity progressively increased from 2021 onward, consistent with the rising phase of SC25, with the most intense events concentrated in early 2023.

Of the 14 events, eight are classified as G2 ($Kp_{max} = 6.3 - 6.6$), three as G3 ($Kp_{max} = 7.0 - 7.7$) and three as G4 ($Kp_{max} = 8.0 - 8.3$). The Dst index reinforces this classification: the G2 storms produce minimum Dst values ranging from -18 nT to -85 nT, while the G3 and G4 events yield substantially deeper depressions, with the most intense event, 23 April 2023 ($Kp_{max} = 8.3$, G4), reaching a Dst minimum of -165 nT and the consecutive event on 24 April 2023 attaining the deepest depression of the entire study period at -213 nT. The March–April 2023 sequence is particularly noteworthy, as four G3–G4 class storms occurred within a span of 32 days, indicative of a period of elevated solar activity near the SC25 maximum.

A notable exception is the 03 November 2021 event, which satisfies the Kp > 6 criterion ($Kp_{max} = 6.3$, G2) yet the Dst index does not drop below -30 nT throughout the day, with a minimum of only -18 nT. This discrepancy suggests that the ring current enhancement associated with this event was relatively weak despite the elevated Kp, likely reflecting a storm driven primarily by substorm-related auroral currents rather than a sustained ring current injection. Accordingly, storm onset for this event is defined by the Dst minimum hour rather than the standard -30 nT threshold, as described in Section 2.1. The seasonal distribution of events, with seven occurring in spring, two in autumn, two in summer, one in winter and two spanning the summer/autumn transition, reflects the well-known Russell–McPherron effect, whereby the southward component of the interplanetary magnetic field is statistically enhanced near the equinoxes, increasing the geoeffectiveness of solar wind structures (Russell & McPherron, 1973). The quiet reference day (07 May 2022) exhibits Kp values not exceeding 1.66 throughout the day and Dst values remaining within the range -10 to -1 nT, confirming its suitability as a geomagnetically undisturbed baseline for the normalization procedure.

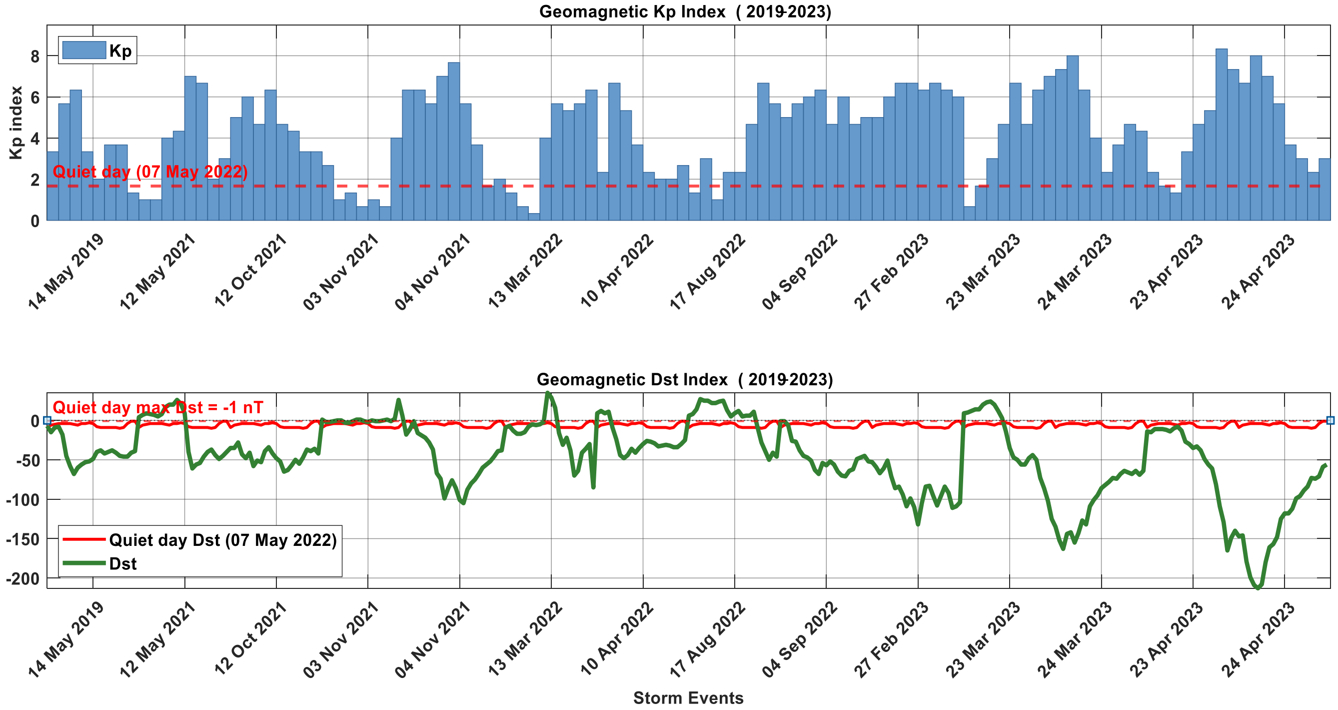

Figure 2. Kp (top panel) and Dst (bottom panel) indices for the geomagnetically disturbed days and one quiet day between 2019 and 2023.

Figure 3 presents the SYM-H index at 1-minute resolution for the same 14 disturbed days and the quiet reference day. Compared to the hourly Dst shown in Figure 2, the SYM-H index reveals finer temporal structure in the storm development, particularly during the sudden storm commencement (SSC) and the main phase onset. For the G4 events of March–April 2023, the SYM-H time series shows rapid main phase deepening rates, with the 23 April 2023 event exhibiting a decrease of approximately 130 nT within a few hours following onset near 12:00 UT and the 24 April 2023 event reaching a minimum SYM-H of -213 nT, the deepest value recorded in the study period. The high cadence of SYM-H also captures brief positive excursions during the initial phase of several events, most notably in the 12 May 2021 and 10 April 2022 storms, reflecting sudden commencement signatures associated with interplanetary shock arrival. For the 03 November 2021 event, consistent with the Dst analysis, the SYM-H trace remains close to baseline throughout the day, with only a modest perturbation in the late evening hours, further supporting the interpretation that this event represents a weak ring current response. The quiet reference day SYM-H values fluctuate within ±10 nT, confirming the absence of any significant geomagnetic disturbance.

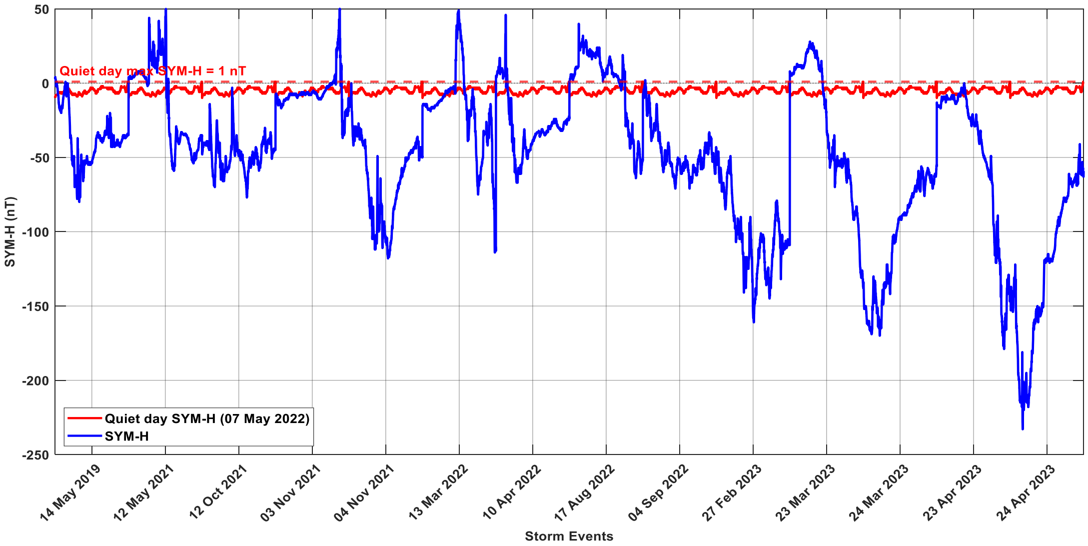

Figure 3. SYM-H index for the geomagnetically disturbed days and one quiet day between 2019 and 2023.

Figure 4 compares the storm-time IONOLAB-TEC ($\boldsymbol{x}_{u;d_s}$, solid blue) with the scaled quiet-day reference ($\boldsymbol{x}^{ref}_{u;d_s}$, dashed red) for all nine stations during the 23 April 2023 geomagnetic storm (G4, $Kp_{max} = 8.3$). Prior to storm onset at approximately 12:00 UT, the two curves are in close agreement across the entire network, validating the pre-storm scaling approach. Following onset, a network-wide positive deviation is initially observed, followed by a transition to predominantly negative values in the post-onset hours, yielding a peak positive $r\Delta TEC$ of +20.5% and a peak negative of −30.9% (Table 3). The negative phase dominates the remainder of the day, with a total negative-phase duration of 13.9 hours compared to only 10.1 hours of positive phase, the most negative-phase-dominant event in the study period despite its G4 classification. This apparently paradoxical result, whereby the most intense storm by Kp does not produce the largest positive TEC enhancement, is consistent with the well-established dependence of the ionospheric storm response on the local time of onset. The storm on 23 April 2023 commenced near local noon over Türkiye (12:00 UT ≈ 14:00–15:00 LT), a timing that favors the composition-driven negative phase over the electric field-driven positive phase, since the disturbance dynamo electric fields that produce TEC enhancements are most effective during post-midnight and morning hours (Fejer & Scherliess, 1997). In contrast, the consecutive event of 24 April 2023, which commenced near midnight (onset_h ≈ 00:00 UT), produced a peak positive $r\Delta TEC$ of +167.6% and a positive phase duration of 19.3 hours, directly illustrating the onset local-time control on storm phase dominance. The supplementary figures for the remaining 13 events confirm this pattern across the full event set.

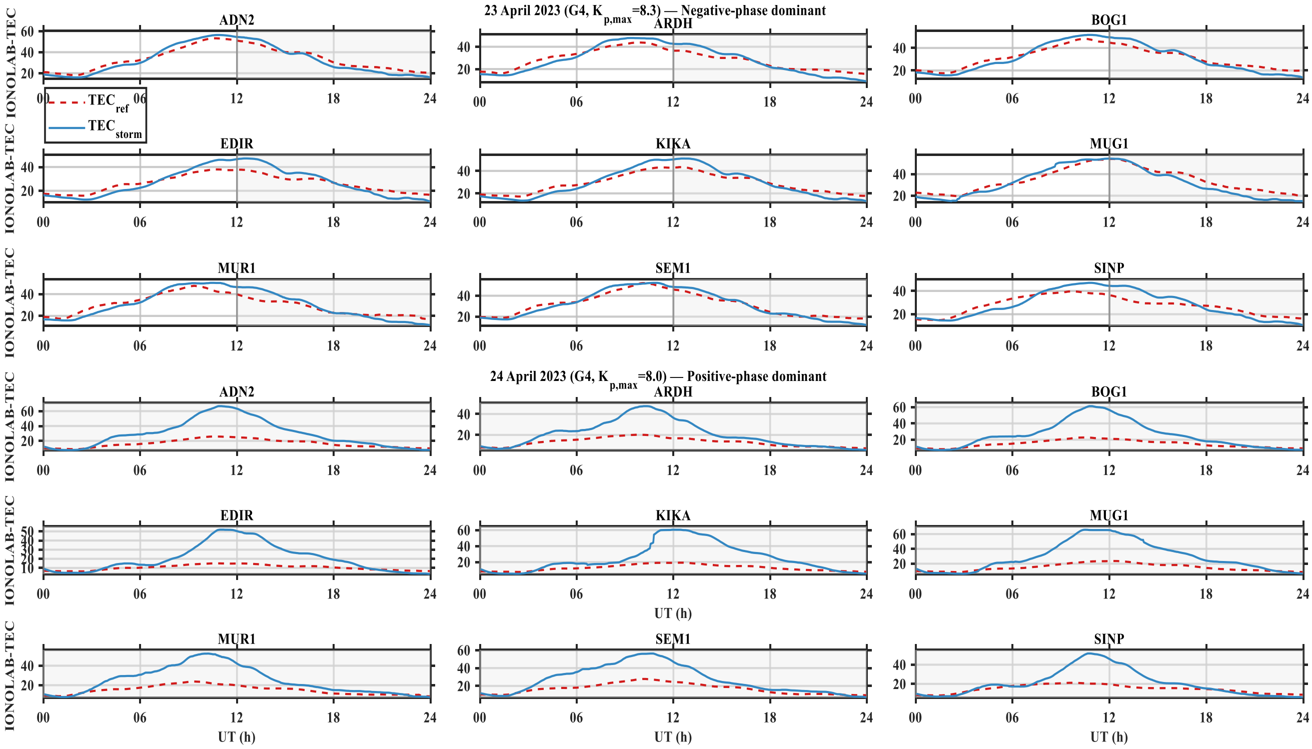

Figure 4. Comparison of storm-time IONOLAB-TEC (TEC_{storm}, solid blue) and scaled quiet-day reference IONOLAB-TEC (TEC_{ref}, dashed red) for the nine GNSS stations during two consecutive G4 geomagnetic storms illustrating contrasting storm phase dominance. Upper panels: 23 April 2023 (G4, Kpmax = 8.3), a negative-phase-dominant event with storm onset near local noon (~12:00 UT). Lower panels: 24 April 2023 (G4, Kpmax = 8.0), a positive-phase-dominant event with storm onset near local midnight (~00:00 UT). Grey shading indicates the post-onset period and the vertical grey line marks the storm onset in each panel. The contrasting behaviors of these consecutive events, which differ only in onset local time, directly illustrate the dominant role of onset timing in controlling ionospheric storm phase dominance.

Table 3. Summary statistics of the ionospheric storm response for each event.

Date	**Class**	**Season**	**Peak $r\Delta TEC^{+}$ (%)**	**Peak $r\Delta TEC^{-}$ (%)**	**Dur⁺ (h)**	**Dur⁻ (h)**	**k (mean ± σ)**
14 May 2019	G2	Spring	+28.9	−26.1	13.2	10.8	0.469 ± 0.044
12 May 2021	G3	Spring	+64.6	−19.8	11.1	12.9	0.533 ± 0.048
12 Oct 2021	G2	Autumn	+41.0	−25.6	12.3	11.7	0.526 ± 0.051
03 Nov 2021	G2	Autumn	+34.8	−31.2	14.1	9.9	0.465 ± 0.034
04 Nov 2021	G3	Autumn	+118.7	−21.7	20.0	4.0	0.504 ± 0.052
13 Mar 2022	G2	Spring	+31.6	−33.7	12.9	11.1	0.717 ± 0.062
10 Apr 2022	G2	Spring	+41.3	−33.6	12.6	11.4	0.913 ± 0.080
17 Aug 2022	G2	Summer	+27.7	−16.4	13.4	10.6	0.857 ± 0.070
04 Sep 2022	G2	Autumn	+30.3	−15.7	18.8	5.2	0.757 ± 0.086
27 Feb 2023	G2	Winter	+197.4	−32.8	21.0	3.0	0.644 ± 0.079
23 Mar 2023	G3	Spring	+42.4	−41.8	10.2	13.8	1.372 ± 0.119
24 Mar 2023	G4	Spring	+140.9	−55.3	12.7	11.3	0.762 ± 0.103
23 Apr 2023	G4	Spring	+20.5	−30.9	10.1	13.9	1.184 ± 0.126
24 Apr 2023	G4	Spring	+167.6	−25.2	19.3	4.7	0.560 ± 0.071

Peak positive and peak negative $r\Delta TEC$ values represent network-mean maxima and minima, respectively. Phase durations are computed as the total time (hours) for which the network-mean $r\Delta TEC$ remains positive or negative. The pre-storm scaling factor k is reported as the mean ± standard deviation across the nine stations.

Figure 5 presents the network-averaged normalized TEC deviation $\overline{r\Delta x_{d_s}}(n)$ with ±1σ envelope for all 14 storm events. Several key features emerge from a systematic inspection of the panels. First, positive storm phases dominate the daytime hours in the majority of events, but the magnitude varies by more than an order of magnitude across the study period. The most extreme positive deviations are recorded on 27 February 2023 (G2, Winter; peak +197.4%) and 24 April 2023 (G4, Spring; peak +167.6%), while the weakest positive response is observed on 17 August 2022 (G2, Summer; peak +27.7%) and 23 April 2023 (G4, Spring; peak +20.5%). This range illustrates that storm intensity class alone is a poor predictor of TEC enhancement magnitude and that onset timing, season and solar activity level all contribute substantially to the observed response. The anomalously large positive deviation of +197.4% on 27 February 2023 warrants particular attention. This event, despite being classified as G2 ($Kp_{max} = 6.6$), occurred in winter with a storm that was already in progress at 00:00 UT (Dst < -30 nT from the start of the observational window), yielding a k-scale factor of 0.644. The low k value reflects the depressed winter ionosphere over Türkiye relative to the May quiet reference day, so that even a moderate positive TEC perturbation appears amplified when expressed as a percentage relative to the scaled reference. This result highlights both the physical role of seasonal background TEC in modulating the apparent storm response magnitude and a methodological sensitivity of the $r\Delta TEC$ metric to events where the storm onset precedes the observational window, a limitation acknowledged for the four events (12 October 2021, 27 February 2023, 24 March 2023, 24 April 2023) for which the one-hour fallback scaling window was applied.

Second, the negative storm phase is most prominent and sustained in the March–April 2023 G3–G4 sequence. The 24 March 2023 event (G4) produces the deepest network-mean negative deviation of the entire study period at -55.3%, with a negative-phase duration of 11.3 hours. The 23 March 2023 event (G3), which preceded it by one day, also exhibits a pronounced negative phase (-41.8%, 13.8 hours), suggesting that residual thermospheric composition changes from the 23 March event may have preconditioned the ionosphere for a deeper negative response on 24 March. Such storm-on-storm compositional conditioning has been documented in previous multi-day storm sequences (Prölss, 1995).

Third, the 04 November 2021 event (G3, Autumn) stands out with an exceptionally long positive phase duration of 20.0 hours and a peak $r\Delta TEC$ of +118.7%, with a correspondingly short negative phase of only 4.0 hours. The storm onset occurred at approximately 05:00 UT (≈ 07:00–08:00 LT over Türkiye), placing it in the early morning sector where prompt penetration electric fields are known to produce sustained daytime positive phases over mid-latitudes (Tsurutani, et al., 2004). The ±1σ envelope is notably narrow for this event compared to the G4 storms, suggesting a spatially coherent positive response across the Anatolian network.

Fourth, the 03 November 2021 event (G2, Autumn; panel d) is the only event in the study period for which the Dst index did not reach the -30 nT threshold, with a minimum Dst of only -18 nT. Despite this weak ring current signature, the ionospheric TEC response is non-negligible at the network level, with a peak positive deviation of +34.8% and a peak negative deviation of -31.2%. The positive phase (14.1 h) dominates, suggesting that magnetospheric energy input via mechanisms other than the symmetric ring current, such as substorm-driven prompt penetration electric fields, may have contributed to the observed TEC enhancement even in the absence of a pronounced main-phase Dst depression. The retention of this event in the analysis is justified on three grounds. First, the event selection criterion adopted in this study is based exclusively on the maximum 3-hourly Kp index exceeding 6, a threshold that this event satisfies (Kpmax = 6.3). Excluding it post hoc on the basis of the Dst threshold would introduce an inconsistency in the selection procedure and constitute a form of confirmation bias toward events with strong ring current signatures. Second, the Kp-Dst decoupling observed here is a well-documented phenomenon in the literature: intense substorm activity can drive Kp to high values through auroral electrojet enhancement without necessarily producing a sustained symmetric ring current injection sufficient to depress Dst below -30 nT (Gonzalez, et al., 1994; Matzka, et al., 2021). This event therefore represents a physically distinct class of geomagnetic disturbance that is legitimately captured by the Kp-based selection criterion. Third, the ionospheric TEC response to this event is non-negligible, with a network-mean peak positive deviation of +34.8% and a peak negative deviation of -31.2%, confirming that magnetospheric energy input, likely via substorm-driven prompt penetration electric fields, did reach the mid-latitude ionosphere over Türkiye despite the weak ring current signature.

Figure 6 presents the pre-storm scaling factor $k_{u;d_s}$ for all station–event pairs. The heatmap reveals two distinct and physically interpretable patterns: a solar cycle trend along the horizontal axis and a seasonal modulation within each year. Regarding the solar cycle trend, all events from 2019 to mid-2021 yield k values in the range 0.46–0.53, well below unity, indicating that the pre-storm TEC background during these SC24-minimum years was roughly half that of the May 2022 quiet reference day. This is consistent with the substantially reduced solar EUV flux during the SC24/SC25 transition minimum, which suppressed photo-ionization rates and depressed the background ionospheric plasma density (Huang, et al., 2016; Liu, et al., 2006). By 2022, k values rise to 0.72–0.91, reflecting the increasing solar flux during the ascending phase of SC25. In early 2023, two events (23 March 2023, $k = 1.372$; 23 April 2023, $k = 1.184$) yield k values exceeding unity, meaning that the pre-storm TEC on those days was already higher than the May 2022 quiet reference, a consequence of the elevated solar activity near the SC25 maximum, which had surpassed the activity level of the reference day by early 2023.

The inter-station spread of k within a given event is small ($\sigma_k = 0.036 - 0.134$, Table 3), confirming spatial coherence of the background TEC across the Anatolian network at the pre-storm timescale. The largest inter-station spread occurs for the 23 March 2023 event ($\sigma_k = 0.126$) and 23 April 2023 ($\sigma_k = 0.134$), both during the late-storm-sequence period when the ionosphere may have been spatially non-uniform due to preceding geomagnetic activity.

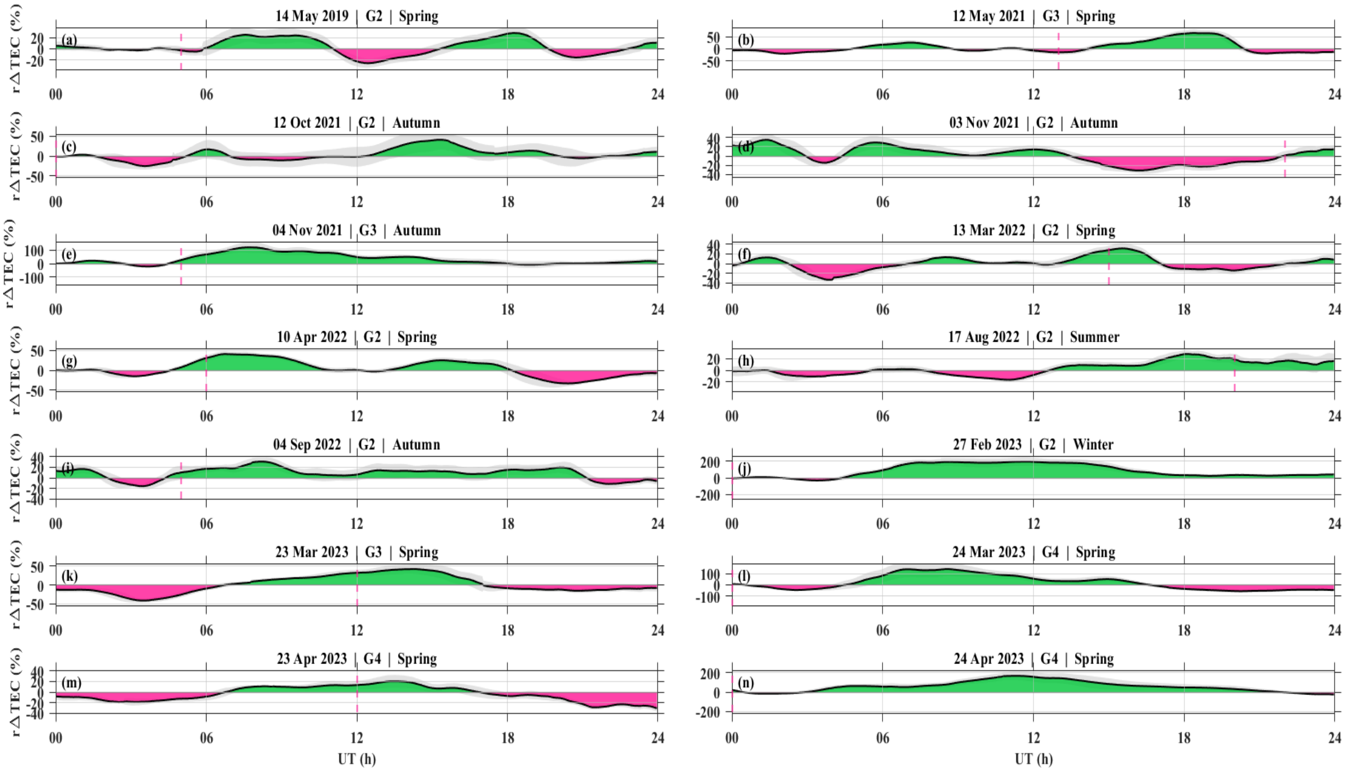

Figure 5. Normalized IONOLAB-TEC deviation, $r\Delta TEC$ (%), for all 14 storm events, computed as the network mean over nine stations (solid black line) with ±1σ envelope (grey shading). Green and red shadings denote positive and negative ionospheric storm phases, respectively. The red dashed vertical line marks the storm onset in each panel.

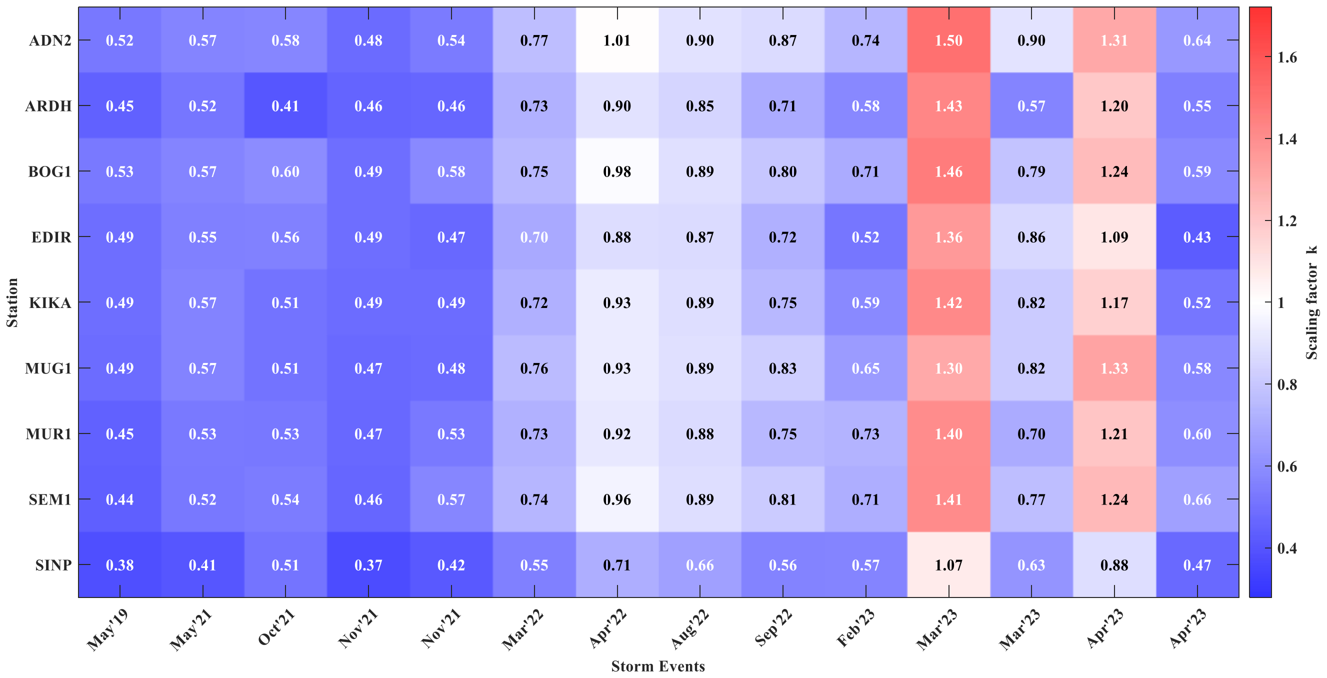

Station	May'19	May'21	Oct'21	Nov'21	Nov'21	Mar'22	Apr'22	Aug'22	Sep'22	Feb'23	Mar'23	Mar'23	Apr'23	Apr'23
ADN2	0.52	0.57	0.58	0.48	0.54	0.77	1.01	0.90	0.87	0.74	1.50	0.90	1.31	0.64
ARDH	0.45	0.52	0.41	0.46	0.46	0.73	0.90	0.85	0.71	0.58	1.43	0.57	1.20	0.55
BOG1	0.53	0.57	0.60	0.49	0.58	0.75	0.98	0.89	0.80	0.71	1.46	0.79	1.24	0.59
EDIR	0.49	0.55	0.56	0.49	0.47	0.70	0.88	0.87	0.72	0.52	1.36	0.86	1.09	0.43
KIKA	0.49	0.57	0.51	0.49	0.49	0.72	0.93	0.89	0.75	0.59	1.42	0.82	1.17	0.52
MUG1	0.49	0.57	0.51	0.47	0.48	0.76	0.93	0.89	0.83	0.65	1.30	0.82	1.33	0.58
MUR1	0.45	0.53	0.53	0.47	0.53	0.73	0.92	0.88	0.75	0.73	1.40	0.70	1.21	0.60
SEM1	0.44	0.52	0.54	0.46	0.57	0.74	0.96	0.89	0.81	0.71	1.41	0.77	1.24	0.66
SINP	0.38	0.41	0.51	0.37	0.42	0.55	0.71	0.66	0.56	0.57	1.07	0.63	0.88	0.47

Figure 6. Pre-storm scaling factor k for each station–event pair. Values greater than 1 indicate higher TEC background during the storm day relative to the quiet reference day (07 May 2022), reflecting seasonal and solar activity differences.

The robustness of the single quiet reference day approach is further supported by the pre-storm agreement observed across the supplementary figures (Figures S1–S13). In each event, the storm-time IONOLAB-TEC and the scaled quiet-day reference converge closely during the pre-onset window, confirming that the scaling factor k effectively absorbs the seasonal and solar-cycle differences in background TEC regardless of the reference day chosen. While a formal sensitivity analysis using alternative quiet days would require additional IONOLAB-TEC retrievals beyond the scope of the present study, the physical consistency of k with independently known solar EUV trends across SC24-SC25 (Huang, et al., 2016; Liu, et al., 2006) provides implicit validation of the normalization procedure. The acknowledged limitation of the percentage-based $r\Delta TEC$ metric for low-k events (2019–2021) does not affect the qualitative characterization of storm phase polarity or duration, which are the primary observational quantities reported herein.

The systematic underestimation of k for the 2019–2021 events has a direct implication for the $r\Delta TEC$ metric: since $TEC_{ref} = k \cdot \boldsymbol{x}_{u;d_q}$ is scaled to a low baseline for these early events, any given absolute TEC perturbation translates into a larger percentage deviation than it would for a 2022–2023 event with a higher background. This cross-cycle asymmetry should be borne in mind when interpreting peak $r\Delta TEC$ values across events from different phases of the solar cycle and underscores the utility of the pre-storm scaling approach adopted in Section 2.1, which anchors the normalization to the observed pre-storm TEC level rather than to a fixed solar activity proxy.

Figure 7 presents the statistical distribution of the peak positive and peak negative deviations across all nine stations, stratified by storm intensity class (panels a–b) and season (panels c–d). Storm intensity dependence (panels a–b): A statistically meaningful progression with storm class is observed for the positive phase: the median peak positive $r\Delta TEC$ increases from +37.1% for G2 events to +66.8% for G3 and +140.1% for G4 and the mean values follow the same ordering (+59.1%, +78.8%, +114.7%). The interquartile range widens substantially from G2 to G4, reflecting the greater event-to-event and station-to-station variability during intense storms. For the negative phase (panel b), the class ordering is less monotonic: G2 events yield a median peak of -31.4%, G3 events -26.0% and G4 events -34.9%. The comparatively shallow G3 negative median is influenced by the 04 November 2021 event, which had an exceptionally dominant positive phase and a very short negative phase (4.0 h), pulling the G3 distribution upward. The wide spread of the G4 box reflects the contrasting behavior of the three G4 events: 24 March 2023 produced the deepest negative phase (-55.3%), while 24 April 2023 produced only -25.2%, with 23 April 2023 intermediate at -30.9%.

It should be noted that the seasonal groups are unequally sampled: spring comprises seven events (n=63 station-event pairs), while summer and autumn each comprise two events (n=18) and winter only one event (n=9). Accordingly, seasonal interpretations for the summer, autumn and winter groups should be treated as indicative rather than statistically definitive and the spring group provides the most robust seasonal characterization. Seasonal dependence (panels c–d): The positive phase analysis (panel c) reveals that winter events exhibit the highest median positive peak (+189.2%), followed by spring (+46.1%), autumn (+41.6%) and summer (+29.6%). However, the winter median is dominated by the single 27 February 2023 event (+197.4%), and the associated box spans an exceptionally wide range due to the combination of the large percentage deviation and the low background TEC discussed in the context of Figure 6. Spring events, by contrast, show the broadest seasonal sample (seven events) and a more representative median. The relatively weak positive response in summer is consistent with the lower occurrence probability of positive ionospheric storms during solstitial periods over mid-latitudes, where the thermospheric composition is less favorable for density enhancements driven by equatorward neutral winds (Mendillo, 2006; Prölss, 1993).

For the negative phase (panel d), spring produces the deepest median (-33.9%) and winter the deepest mean (-38.2%), while summer shows the weakest negative response (median -19.7%). This seasonal ordering is consistent with the greater susceptibility of the spring and winter ionosphere to negative-phase composition changes, where the increased O/N_2 depletion driven by storm-time Joule heating and Lorentz forcing at high latitudes propagates equatorward more efficiently during winter and spring due to the prevailing thermospheric circulation patterns (Fuller-Rowell, et al., 1994). The summer suppression of both phases is in agreement with findings from previous studies of mid-latitude ionospheric storms in the Eastern Mediterranean and Balkan region (Karatay, et al., 2017; Karatay, 2020a; Karatay, 2020b; Karatay, 2020c).

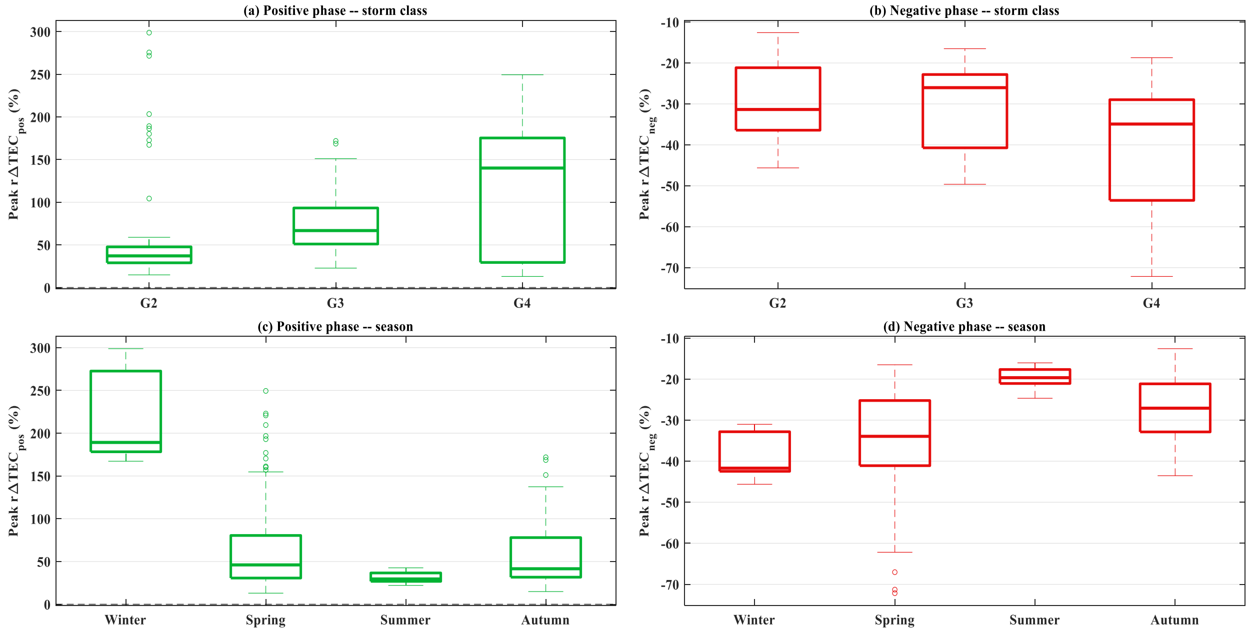

Figure 7. Box plots of peak positive (a, c) and peak negative (b, d) $r\Delta TEC$ (%) grouped by storm intensity class (a, b) and season (c, d). Each box represents the distribution across all nine stations within the group. The number of station-event data points contributing to each box is as follows, storm class: G2: n=72, G3: n=27, G4: n=27; season: Spring: n=63, Summer: n=18, Autumn: n=18, Winter: n=9. Whiskers extend to 1.5 times the interquartile range.

Collectively, the results presented in this section demonstrate that the ionospheric response over Türkiye during geomagnetic storms is governed by a complex interplay of storm intensity, onset local time, season and background solar activity level, none of which acts independently. While storm intensity class provides a first-order indicator of the expected TEC perturbation magnitude, with G4 events producing median peak positive deviations approximately four times larger than G2 events, the wide intra-class variability observed in both the positive and negative phases confirms that Kp or storm class alone is insufficient to characterize the ionospheric storm response at a specific location. The onset local time emerges as a particularly critical modulator, as illustrated by the contrasting behavior of the consecutive 23 and 24 April 2023 G4 events, where a difference of approximately 12 hours in onset timing reversed the dominant storm phase from negative to positive. Seasonal effects further modulate the response through changes in thermospheric composition, background plasma density and the efficiency of prompt penetration electric fields, with spring events producing the most pronounced and consistent positive phases over the Anatolian network. The pre-storm scaling analysis reveals a clear solar cycle imprint on the background TEC, with k values increasing from approximately 0.47 during the SC24 minimum to above 1.3 during the SC25 ascending phase, a factor that directly influences the apparent magnitude of normalized TEC deviations and must be accounted for in any multi-year comparative study. Taken together, these findings provide a comprehensive observational baseline for mid-latitude ionospheric storm morphology over Türkiye during the SC24–SC25 transition period and highlight the value of spatially distributed GNSS networks combined with observation-based normalization for characterizing storm-time ionospheric variability.

4. Conclusion

This study provides a detailed characterization of the ionospheric storm response over Türkiye during 14 geomagnetically disturbed days (G2–G4 class) between January 2019 and June 2023, using high-resolution IONOLAB-TEC estimates derived from nine TNPGN-Active GNSS stations. By applying an observation-driven pre-storm scaling procedure anchored to a single quiet reference day (07 May 2022), the analysis successfully isolated storm-induced TEC deviations while effectively accounting for seasonal and solar-cycle differences in background ionization levels across the SC24 minimum to SC25 ascending phase transition.

The results demonstrate that the mid-latitude ionosphere over the Anatolian region exhibits highly variable responses governed by a complex interplay of multiple drivers. Storm intensity (Kp/Dst) offers a first-order control on the magnitude of perturbations, with G4 events generally producing larger peak positive deviations than G2 events. However, intra-class variability is substantial, underscoring that geomagnetic indices alone are insufficient predictors. The local time of storm onset emerges as a dominant modulator: events commencing near local noon favor composition-driven negative phases, whereas midnight-to-morning onsets promote prolonged electric field-driven positive phases, as clearly illustrated by the contrasting behaviors of the consecutive 23 and 24 April 2023 G4 storms.

Seasonal effects further shape the response, with spring events showing the most consistent and pronounced positive phases, winter conditions amplifying relative enhancements due to lower background TEC and summer periods suppressing both phases due to unfavorable thermospheric composition.

The pre-storm scaling factor analysis reveals a clear solar-cycle imprint, with background TEC roughly doubling from the deep SC24 minimum (2019–mid-2021) to the more active early SC25 period (2022–2023). This background modulation directly influences the apparent percentage deviations ($r\Delta TEC$), highlighting the importance of observation-based normalization over reliance on fixed solar proxies in multi-year studies. Network-averaged statistics and phase-duration metrics further confirm spatial coherence across the nine stations while capturing regional gradients over nearly 18° of longitude in the Eastern Mediterranean sector. These findings contribute to a better understanding of mid-latitude ionospheric dynamics in a longitude sector that has been relatively underrepresented in global storm-time statistics. Practically, the observed TEC perturbations and their dependence on onset timing and season have direct implications for GNSS error mitigation, precise positioning and space weather forecasting services in Türkiye and surrounding regions. As Solar Cycle 25 progresses toward its maximum, the frequency of intense geomagnetic events is expected to rise, increasing the operational relevance of such regional benchmarks.

Future work could extend this analysis by incorporating additional TNPGN-Active stations for finer spatial resolution, integrating ionosonde and satellite data for multi-instrument validation, or developing empirical models that incorporate onset local time and pre-storm background as explicit inputs. Overall, this study demonstrates the value of dense, continuously operating GNSS networks combined with robust normalization techniques for advancing both scientific insight and practical space weather applications in mid-latitude regions.

Conflict of Interest

The authors declare that they have no conflict of interest.

Disclosure of Generative AI Use

The authors used a generative artificial intelligence (AI) tool solely to assist in improving the language and drafting of the Introduction section of this manuscript. The AI tool was not used for study design, data collection, data analysis, interpretation of results, or the generation of scientific conclusions. All content was carefully reviewed, revised where necessary, and approved by the authors, who take full responsibility for the final content of the manuscript.

References

Akala, A., Afolabi, R., & Otsuka, Y. (2023). Responses of the African-European equatorial-, low-, mid-, and high-latitude ionosphere to geomagnetic storms of 2013, 2015 St Patrick’s Days, 1 June 2013, and 7 October 2015. *Advances in Space Research*, *72*(3), 775-789. https://doi.org/10.1016/j.asr.2022.10.029

Arikan, F., Erol, C. B., & Arikan, O. (2003). Regularized estimation of vertical total electron content from Global Positioning System data. *Journal of Geophysical Research: Space Physics*, *108*(A12), 1-20. https://doi.org/10.1029/2002JA009605

Arikan, F., Nayir, H., Sezen, U., & Arikan, O. (2008). Estimation of single station interfrequency receiver bias using GPS-TEC. *Radio Science*, *43*(4), 1-13. https://doi.org/10.1029/2007RS003785

Arikan, F., Shukurov, S., Tuna, H., Arikan, O., & Gulyaeva, T. (2016). Performance of GPS slant total electron content and IRI-Plas-STEC for days with ionospheric disturbance. *Geodesy and Geodynamics*, *7*(1), 1-10. https://doi.org/10.1016/j.geog.2015.12.009

Campuzano, S., Delgado-Gómez, F., Migoya-Orué, Y., Rodríguez-Caderot, G., Herraiz-Sarachaga, M., & Radicella, S. (2023). Study of ionosphere irregularities over the iberian peninsula during two moderate geomagnetic storms using GNSS and ionosonde observations. *Atmosphere*, *14*(2), 1-16. https://doi.org/10.3390/atmos14020233

Doğanalp, S., & Köz, İ. (2024). Monitoring ionospheric and atmospheric conditions during the 2023 Kahramanmaraş earthquake period. *Atmosphere*, *15*(12), 1542. https://doi.org/10.3390/atmos15121542

Erken, F., Karatay, S., & Cinar, A. (2019). Spatio-temporal prediction of ionospheric total electron content using an adaptive data fusion technique. *Geomagnetism and Aeronomy*, *59*, 971-979. https://doi.org/10.1134/S001679321908005X

Fagundes, P. R., Cardoso, F. A., Fejer, B. G., Venkatesh, K., Ribeiro, B. A., & Pillat, V. G. (2016). Positive and negative GPS-TEC ionospheric storm effects during the extreme space weather event of March 2015 over the Brazilian sector. *Journal of Geophysical Research: Space Physics*, *121*(6), 5613-5625. https://doi.org/10.1002/2015JA022214

Fejer, B. G., & Scherliess, L. (1997). Empirical models of storm time equatorial zonal electric fields. *Journal of Geophysical Research: Space Physics*, *102*(A11), 24047-24056. https://doi.org/10.1029/97JA02164

Fuller-Rowell, T. J., Codrescu, M. V., & R. J. Moffett, S. Q. (1994). Response of the thermosphere and ionosphere to geomagnetic storms. *Journal of Geophysical Research: Space Physics*, *99*(A3), 3893-3914. https://doi.org/10.1029/93JA02015

GFZ. (1956). *GFZ helmholtz centre for geosciences*. Retrieved Aug 04, 2025, from https://www-app3.gfz-potsdam.de/kp_index/Kp_ap_since_1932.txt

Ghafar, M. M., Mohammed, D. H., Salh, H., Dleer, S., & Külahcı, S. M. (2024). Ionospheric Whispers of the Earth's tremors: Decoding TEC Mysteries in the East Anatolian Fault Zone. *Geomagnetism and Aeronomy*, *64*, 772-780. https://doi.org/10.1134/S0016793223600960

Gonzalez, W. D., Joselyn, J. A., Kamide,Y. H., Kroehl,W., Rostoker,G., Tsurutani,B. T., & Vasyliunas, V. M. (1994). What is a geomagnetic storm? *Journal of Geophysical Research: Space Physics*, *99*(A4), 5771-5792. https://doi.org/10.1029/93JA02867

Gulyaeva, T. L., Arikan, F., Hernandez-Pajares, M., & Veselovsky, I. S. (2014). North-south components of the annual asymmetry in the ionosphere. *Radio Science*, *49*(7), 485-496. https://doi.org/10.1002/2014RS005401

Gulyaeva, T., & Stanislawska, I. (2005). Night−day imprints of ionospheric slab thickness during geomagnetic storm. *Journal of Atmospheric and Solar-Terrestrial Physics*, *67*(14), 1307-1314. https://doi.org/10.1016/j.jastp.2005.07.006

Hajra, R., Franco, A. M., Echer, E., & Bolzan, M. J. (2021). Long-Term variations of the geomagnetic activity: A comparison between the strong and weak solar activity cycles and implications for the space climate. *Journal of Geophysical Research: Space Physics*, *126*(4), 1-14. https://doi.org/10.1029/2020JA028695

Haralambous, H., & Makrominas, M. (2024). Validation of the European Ionosonde Service nowcasting foF2 maps over the eastern Mediterranean. *Advances in Space Research*, *73*(3), 1799-1813. https://doi.org/10.1016/j.asr.2023.10.035

Hernández-Pajares, M., Juan, J. M., Sanz, J., Aragón-Àngel, À., García-Rigo, A., Salazar, D., & Escudero, M. (2011). The ionosphere: Effects, GPS modeling and the benefits for space geodetic techniques. *Journal of Geodesy*, *85*, 887-907. https://doi.org/10.1007/s00190-011-0508-5

Huang, C.-S., Foster, J. C., & Kelley, M. C. (2005). Long-duration penetration of the interplanetary electric field to the low-latitude ionosphere during the main phase of magnetic storms. *Journal of Geophysical Research: Space Physics*, *110*(A11), 1-13. https://doi.org/10.1029/2005JA011202

Huang, J., Hao, Y., Zhang, D., & Xiao, Z. (2016). Changes of solar extreme ultraviolet spectrum in solar cycle 24. *Journal of Geophysical Research: Space Physics*, *121*(7), 6844-6854. https://doi.org/10.1002/2015JA022231

Jakowski, N., Béniguel, Y., & Franceschi, G. D. (2012). Monitoring, tracking and forecasting ionospheric perturbations using GNSS techniques. *Journal of Space Weather and Space Climate*, *2*(A22), 1-14. https://doi.org/10.1051/swsc/2012022

Javaraiah, J. (2022). Long-term variations in solar activity: Predictions for amplitude and north–south asymmetry of solar cycle 25. *Solar Physics*, *297*, 33. https://doi.org/10.1007/s11207-022-01956-z

Jin, S., Jin, R., & Kutoglu, H. (2017). Positive and negative ionospheric responses to the March 2015 geomagnetic storm from BDS observations. *Journal of Geodesy*, *91*, 613-626. https://doi.org/10.1007/s00190-016-0988-4

Karatay, S. (2020a). Detection of the ionospheric disturbances on GPS-TEC using Differential Rate Of TEC (DROT) algorithm. *Advances in Space Research*, *65*(10), 2372-2390. https://doi.org/10.1016/j.asr.2020.01.042

Karatay, S. (2020b). Estimation of frequency and duration of ionospheric disturbances over Turkey with IONOLAB-FFT algorithm. *Journal of Geodesy*, *94*, 89. https://doi.org/10.1007/s00190-020-01416-1

Karatay, S. (2020c). Temporal variations of the ionospheric disturbances due to the seasonal variability over Turkey using IONOLAB-FFT algorithm. *Geodesy and Geodynamics*, *11*(3), 182-191. https://doi.org/10.1016/j.geog.2019.12.002

Karatay, S., Cinar, A., & Arikan, F. (2017). Ionospheric responses during equinox and solstice periods over Turkey. *Advances in Space Research*, *60*(9), 1958-1967. https://doi.org/10.1016/j.asr.2017.07.038

Koroglu, M., & Arikan, F. (2025). Statistical analysis of regional STEC gradient trends for midlatitude ionosphere. *Geodesy and Geodynamics*, *16*(1), 7-28. https://doi.org/10.1016/j.geog.2024.04.006

Lei, J., Thayer, J. P., Forbes, J. M., Wu, Q., She, C., Wan, W., & Wang, W. (2008). Ionosphere response to solar wind high-speed streams. *Geophysical Research Letters*, *35*(19), 1-5. https://doi.org/10.1029/2008GL035208

Liu, L., Wan, W., Ning, B., Pirog, O. M., & Kurkin, V. I. (2006). Solar activity variations of the ionospheric peak electron density. *Journal of Geophysical Research: Space Physics*, *111*(A8), 1-13. https://doi.org/10.1029/2006JA011598

Lu, G., Richmond, A. D., Emery, B. A., & Roble, R. G. (1995). Magnetosphere-ionosphere-thermosphere coupling: Effect of neutral winds on energy transfer and field-aligned current. *Journal of Geophysical Research: Space Physics*, *100*(A10), 19643-19659. https://doi.org/10.1029/95JA00766

Lyon, J. G. (2000). The solar wind-magnetosphere-ionosphere system. *Science*, *288*(5473), 1987-1991. https://doi.org/10.1126/science.288.5473.1987

Maruyama, N., Richmond, A. D., Fuller-Rowell, T. J., Codrescu, M. V., Sazykin, S., Toffoletto, F. R., Spiro, R. W., & Millward, G. H. (2005). Interaction between direct penetration and disturbance dynamo electric fields in the storm-time equatorial ionosphere. *Geophysical Research Letters*, *32*(17), 1-4. https://doi.org/10.1029/2005GL023763

Matzka, J., Stolle, C., Yamazaki, Y., Bronkalla, O., & Morschhauser, A. (2021). The geomagnetic kp index and derived indices of geomagnetic activity. *Space Weather*, *19*(5), e2020SW002641. https://doi.org/10.1029/2020SW002641

Mendillo, M. (2006). Storms in the ionosphere: Patterns and processes for total electron content. *Reviews of Geophysics*, *44*(4), 1-47. https://doi.org/10.1029/2005RG000193

Mishin, V. M., Mishin, V. V., Kurikalova, M. A., Sapronova, L. A., & Karavaev, Y. A. (2019). Positive and negative feedbacks in the magnetosphere-ionosphere coupling. *Journal of Atmospheric and Solar-Terrestrial Physics*, *187*, 10-21. https://doi.org/10.1016/j.jastp.2019.03.002

Nakano, S., & Iyemori, T. (2005). Storm-time field-aligned currents on the nightside inferred from ground-based magnetic data at midlatitudes: Relationships with the interplanetary magnetic field and substorms. *Journal of Geophysical Research: Space Physics*, *110*(A7), 1-13. https://doi.org/10.1029/2004JA010737

Nayir, H., Arikan, F., Arikan, O., & Erol, C. B. (2007). Total electron content estimation with reg-est. *Journal of Geophysical Research: Space Physics*, *112*(A11), 1-11. https://doi.org/10.1029/2007JA012459

Paul, K. S., Haralambous, H., Moses, M., & Tripathi, S. C. (2025). Effects of the October 2024 storm over the global ionosphere. *Remote Sensing*, *17*(13), 2329. https://doi.org/10.3390/rs17132329

Pica, E., Spogli, L., Cesaroni, C., Alfonsi, L., Haralambous, H., Vallianatos, F., De Franceschi, G., Romano, V., & Marcocci, C. (2025). Assessing the ionospheric scintillations occurrence on L-band in the southern Mediterranean sector. *Advances in Space Research*, *75*(1), 837-855. https://doi.org/10.1016/j.asr.2024.10.032

Pietrella, M., Pignalberi, A., Pezzopane, M., Pignatelli, A., Azzarone, A., & Rizzi, R. (2018). A comparative study of ionospheric IRIEup and ISP assimilative models during some intense and severe geomagnetic storms. *Advances in Space Research*, *61*(10), 2569-2584. https://doi.org/10.1016/j.asr.2018.02.026

Prölss, G. W. (1993). Common origin of positive ionospheric storms at middle latitudes and the geomagnetic activity effect at low latitudes. *Journal of Geophysical Research: Space Physics*, *98*(A4), 5981-5991. https://doi.org/10.1029/92JA02777

Prölss, G. W. (1995). Ionospheric F-region storms. In H. Volland (Ed.), *Handbook of atmospheric electrodynamics* (pp. 195-248). CRC Press.

Pudovkin, M. I. (1974). Electric fields and currents in the ionosphere. *Space Science Reviews*, *16*, 727-770. https://doi.org/10.1007/BF00182599

Ren, X., Zhang, X., Xie, W., Zhang, K., Yuan, Y., & Li, X. (2016). Global ionospheric modelling using multi-GNSS: BeiDou, Galileo, GLONASS and GPS. *Scientific Reports*, *6*, 33499. https://doi.org/10.1038/srep33499

Richardson, I. G. (2013). Geomagnetic activity during the rising phase of solar cycle 24. *Journal of Space Weather and Space Climate*, *3*, 1-11. https://doi.org/10.1051/swsc/2013031

Ridley, A., Deng, Y., & Tóth, G. (2006b). The global ionosphere–thermosphere model. *Journal of Atmospheric and Solar-Terrestrial Physics*, *68*(8), 839-864. https://doi.org/10.1016/j.jastp.2006.01.008

Ridley, A., Zeeuw, D. D., Manchester, W., & Hansen, K. (2006a). The magnetospheric and ionospheric response to a very strong interplanetary shock and coronal mass ejection. *Advances in Space Research*, *38*(2), 263-272. https://doi.org/10.1016/j.asr.2006.06.010

Rishbeth, H., & Garriott, O. K. (1969). *Introduction to ionospheric physics.* Academic Press.

Russell, C. T., & McPherron, R. L. (1973). Semiannual variation of geomagnetic activity. *Journal of Geophysical Research*, *78*(1), 92-108. https://doi.org/10.1029/JA078i001p00092

Şentürk, E. (2020). Investigation of global ionospheric response of the severe geomagnetic storm on June 22-23, 2015 by GNSS-based TEC observations. *Astrophysics and Space Science*, *365*, 110. https://doi.org/10.1007/s10509-020-03828-z

Sojka, J. J., Rasmussen, C. E., & Schunk, R. W. (1986). An interplanetary magnetic field dependent model of the ionospheric convection electric field. *Journal of Geophysical Research: Space Physics*, *91*(A10), 11281-11290. https://doi.org/10.1029/JA091iA10p11281

Sugiura, M. (1964). *Hourly values of equatorial Dst for the IGY.* Pergamon Press.

Tsurutani, B., Mannucci, A., Iijima, B., Abdu, M. A., Sobral, J. H., Gonzalez, W., & Vasyliunas, V. M. (2004). Global dayside ionospheric uplift and enhancement associated with interplanetary electric fields. *Journal of Geophysical Research: Space Physics*, *109*(A8), 1-16. https://doi.org/10.1029/2003JA010342

Upton, L. A., & Hathaway, D. H. (2023). Solar cycle precursors and the outlook for cycle 25. *Journal of Geophysical Research: Space Physics*, *128*(10), e2023JA031681. https://doi.org/10.1029/2023JA031681

Vaishnav, R., Jacobi, C., & Berdermann, J. (2019). Long-term trends in the ionospheric response to solar extreme-ultraviolet variations. *Annales Geophysicae*, *37*(6), 1141-1159. https://doi.org/10.5194/angeo-37-1141-2019

Vasyliūnas, V. M., & Song, P. (2005). Meaning of ionospheric Joule heating. *Journal of Geophysical Research: Space Physics*, *110*(A2), 1-8. https://doi.org/10.1029/2004JA010615

Wang, W., Lei, J., Burns, A. G., Solomon, S. C., Wiltberger, M., Xu, J., Zhang, Y., Paxton, L., & Coster, A. (2010). Ionospheric response to the initial phase of geomagnetic storms: Common features. *Journal of Geophysical Research: Space Physics*, *115*(A7), 1-18. https://doi.org/10.1029/2009JA014461

Watari, S. (2017). Geomagnetic storms of cycle 24 and their solar sources. *Earth, Planets and Space*, *69*, 70. https://doi.org/10.1186/s40623-017-0653-z

WDC. (1957). *WDC for geomagnetism, Kyoto*. Retrieved Aug 04, 2025, from https://wdc.kugi.kyoto-u.ac.jp///dstae///wwwtmp/WWW_dstae03340870.dat

Wehmeyer, J., Tomikawa, Y., Nishiyama, T., Ogawa, Y., & Franco-Diaz, E. (2026). Poleward disturbances in thermospheric winds during the 3–4 November 2021 geomagnetic storm. *Journal of Geophysical Research: Space Physics*, *131*(2), e2025JA034544. https://doi.org/10.1029/2025JA034544

Yasyukevich, A., Medvedeva, I., Sivtseva, V., Chernigovskaya, M., Ammosov, P., & Gavrilyeva, G. (2020). Strong interrelation between the short-term variability in the ionosphere, upper mesosphere, and winter polar stratosphere. *Remote Sensing*, *12*(10), 1588. https://doi.org/10.3390/rs12101588

Yeeram, T. (2024). The effects of solar radiation and geomagnetic disturbance during consecutive 27-day recurrent geomagnetic storms on variations of equatorial ionospheric parameters and spread F. *Astrophysics and Space Science*, *369*, 62. https://doi.org/10.1007/s10509-024-04327-1

Yi Liu, C. Z., Xu, T., Tang, Q., Deng, Z., Chen, G., & Wang, Z. (2021). Review of ionospheric irregularities and ionospheric electrodynamic coupling in the middle latitude region. *Earth and Planetary Physics*, *5*(5), 462-482. https://doi.org/10.26464/epp2021025

Yu, Y., & Ridley, A. J. (2009). Response of the magnetosphere-ionosphere system to a sudden southward turning of interplanetary magnetic field. *Journal of Geophysical Research: Space Physics*, *114*(A3), 1-10. https://doi.org/10.1029/2008JA013292